

Theory, simulation, fabrication, and characterization of Galois scattering plates for the optical and the THz spectral range

Cite as: AIP Advances 11, 065130 (2021); <https://doi.org/10.1063/5.0053843>

Submitted: 16 April 2021 . Accepted: 02 June 2021 . Published Online: 21 June 2021

 Henning Fouckhardt,  Christoph Doering,  Michael Jaax, and  Bert Laegel



View Online



Export Citation



CrossMark

Call For Papers!

AIP Advances

SPECIAL TOPIC: Advances in
Low Dimensional and 2D Materials

Theory, simulation, fabrication, and characterization of Galois scattering plates for the optical and the THz spectral range

Cite as: AIP Advances 11, 065130 (2021); doi: 10.1063/5.0053843

Submitted: 16 April 2021 • Accepted: 2 June 2021 •

Published Online: 21 June 2021



View Online



Export Citation



CrossMark

Henning Fouckhardt,^{1,a)}  Christoph Doering,¹  Michael Jaax,¹  and Bert Laegel² 

AFFILIATIONS

¹Integrated Optoelectronics and Microoptics Research Group, Physics Department, Technische Universität Kaiserslautern (TUK), P.O. Box 3049, D-67653 Kaiserslautern, Germany

²Nanostructuring Center (NSC), Physics Department, Technische Universität Kaiserslautern (TUK), P.O. Box 3049, D-67653 Kaiserslautern, Germany

^{a)}Author to whom correspondence should be addressed: fouckhar@physik.uni-kl.de

ABSTRACT

Scattering and scattering plates have a large diversity of applications. Scattering of optical and THz electromagnetic waves can be performed with Galois scattering plates, which had found applications in acoustics first (i.e., with sound waves in concert hall acoustics). For binary Galois scattering plates, the single scattering entities, i.e., mesas (for a binary 1) or voids (for a binary 0), have characteristic lateral dimensions of half the wavelength of the electromagnetic waves to be scattered. Their optimal height is a quarter of the wavelength for plates used in reflection. Meanwhile, not too elaborate lithographic techniques allow for the implementation of Galois plates for the THz range and even for the visible spectral range. We had reported on such scattering plates before. However, in this paper, also the mathematical concept is described and the fabrication technologies are emphasized. In contrast to the case of scattering plates with irregular surface morphologies, Galois plate scattering is not diffuse, but there are many scattering/diffraction orders.

© 2021 Author(s). All article content, except where otherwise noted, is licensed under a Creative Commons Attribution (CC BY) license (<http://creativecommons.org/licenses/by/4.0/>). <https://doi.org/10.1063/5.0053843>

I. INTRODUCTION

Optical scattering plates have gained increasing interest in the last decade due to a variety of possible very specific applications—ranging from scattering standards for virtual surfaces in computer game programming to provision of privacy in parts of large halls.^{1,2} In addition, since THz technology is gaining momentum,^{3–8} THz scattering plates might enrich the THz toolbox.

Typically, scattering plates have surfaces with specific roughness morphologies. On the one hand, the latter can be irregular/statistical and produced by self-masking during a dry-etch process.^{9–13} On the other hand, they can be regular and lithographically structured using an etch mask.^{2,14–17} In Refs. 14–16 as well as partially in Refs. 2 and 17, the pattern follows a binary sequence constructed using the binary Galois number field $GF(2^m)$.^{18–20} The latter

is transformed from a one-dimensional (1D) to a two-dimensional (2D) pattern with the help of the Sino representation, which stems from the Chinese remainder theorem (CRT).¹⁸

In Refs. 2 and 17, among other concepts, metallized Galois structures have been used in combination with microfluidics to improve optical sensing of refractive index changes, especially utilizing the *plasmonic* properties of those structures.

We had reported on our earlier work on Galois plates in Refs. 14–16, but here we also explain the mathematical foundations and their implications for the design. Moreover, the fabrication technologies are described in detail.

We have implemented 2D Galois scattering plates for the THz range as well as for the visual spectral range, employing photolithographical as well as e-beam-lithographical techniques, respectively. Our experimental results, which have been achieved for reflective Galois plates, verify the usefulness of the concept. The scattered

radiation is not diffusely spread but rather distributed over a large number of scattering maxima (i.e., diffraction orders) over a large solid angle, with the number of orders depending on the power m of the binary-numbered Galois field $GF(2^m)$ and on the ratio of lateral feature width d and wavelength λ .

II. MATHEMATICS OF GALOIS FIELDS (SEE REF. 18)

Binary Galois number fields are explained here because surface reliefs, which show mesas according to the logical 1's of such sequences, are used further on in this contribution. Taking λ as the vacuum wavelength of the electromagnetic radiation, the mesas should ideally have a width of $d = \lambda/2$ and a height of $h = \lambda/4$ for reflective scattering plates with a top metal coating. At least for optical frequencies, this still constitutes a technological challenge.

A. Mathematical groups and finite number fields

A *group* is a non-empty set G with a mapping $G \diamond G \rightarrow G$ of any two elements a and b of the group, i.e., $a \diamond b$, onto another element of G . The group is associative

$$(a \diamond b) \diamond c = a \diamond (b \diamond c), \tag{1a}$$

and there is an identity element e with

$$a \diamond e = e \diamond a = a, \tag{1b}$$

and an inverse element a^{-1} with

$$a \diamond a^{-1} = a^{-1} \diamond a = e. \tag{1c}$$

The group will be called Abelian if commutativity exists,

$$a \diamond b = b \diamond a. \tag{1d}$$

Moreover, the group will be called cyclic if it contains a primitive element p such that any element a of the group can be written as a natural-numbered power m of p ,

$$p^m = a. \tag{2}$$

A *number field* contains both an additive group (+) and a multiplicative group (\cdot). The multiplicative group includes all the field elements that are not the additive identity (the zero element). The latter cannot be an element of the multiplicative group because it cannot have an inverse element (whose existence is required for any group element).

The operations + and \cdot have to be distributive, i.e.,

$$a \cdot (b + c) = a \cdot b + a \cdot c, \tag{3a}$$

$$(a + b) \cdot c = a \cdot c + b \cdot c. \tag{3b}$$

If the set G is finite, the number field will be called finite, too, or a Galois field.

In this chapter, we use a binary Galois field $GF(2^4)$ exemplarily, i.e., a field with $2^4 - 1 = 15$ four-tuples of binary numbers (1 or 0) plus the zero element 0000. In our experiments, we have also used structures, which represent a field $GF(2^8)$ with $2^8 - 1$ eight-tuples, $GF(2^{10})$ with $2^{10} - 1$ ten-tuples, or even $GF(2^{16})$ with $2^{16} - 1$ sixteen-tuples.

B. Finite number fields of the form $GF(2^m)$

In this article, we are especially interested in residue fields. A residue Galois field is mainly defined by the following operations:

$$a + b = c \text{ mod } p, \tag{4a}$$

$$a \cdot b = c \text{ mod } p \tag{4b}$$

(mod = modulo). In this case, the result of addition/multiplication is the residue or remainder of the *interim* result *divided* by p . The notation $GF(p)$ shall be used only for these residue Galois fields from now on throughout this paper.

The simplest example of such a field is $GF(2)$, which only contains the binary numbers 0 and 1 (for a *binary residue* field, *subtraction* is identical to addition).

In the case of $GF(2^m)$ with $m = 4$, there are 16 elements/ four-tuples (including the zero element) of the number field, i.e., (0000), (0001), (0010), (0100), (1000), (0011), (0110), (1100), (1001), (0101), (1010), (0111), (1110), (1011), (1101), and (1111).

The addition is defined column-wise, which, e.g., gives (1100) + (1111) = (0011). Addition is not the binary addition with carryovers due to the residue arithmetic, the carryovers are ignored.

The multiplication is defined in the following way: The exemplary four-tuples are considered as polynomials (here, with the least significant bit on the far right), e.g., 0011 = $0 \cdot x^3 + 0 \cdot x^2 + 1 \cdot x^1 + 1 \cdot x^0$. Then, multiplication means the multiplication of polynomials *modulo* a given primitive (here binary) polynomial $\mu(x)$ over $GF(p)$ of degree $m = 4$. In order to have an inverse in $GF(2^m)$, the polynomial $\mu(x)$ has to be irreducible. In a set of polynomials, an irreducible polynomial is the equivalent to a prime number in a set of numbers.

In the case of $GF(2^4)$, there are three irreducible polynomials; here, we mention and use just $\mu(x) = x^4 + x + 1$. In Ref. 21, all primitive binary irreducible polynomials are listed up to a degree of 168.

To give an example for multiplication in $GF(2^4)$, we take the four-tuples (1001) and (0110),

$$\begin{aligned} (1001) \cdot (0110) \text{ mod } \mu(x) &= (x^3 + 1) \cdot (x^2 + 1) \text{ mod } \mu(x) \\ &= (x^5 + x^4 + x^2 + x) \text{ mod } (x^4 + x + 1) \\ &= x^5 + x^2 - 1 = x^5 + x^2 + 1. \end{aligned} \tag{4c}$$

Calculating the remainder mod μ is the same as setting the irreducible polynomial to 0. This means that $x^4 = -(1 + x) = (1 + x)$ (neglecting the minus sign because we are using a binary number

field). Thus, the multiplication example from Eq. (4c) can be pursued further,

$$\begin{aligned}
 x^5 + x^2 + 1 &= xx^4 + x^2 + 1 = x(1 + x) + x^2 + 1 = x + x^2 + x^2 + 1 \\
 &= x + 2x^2 + 1 \stackrel{\text{binary}}{\equiv} x + 0x^2 + 1 = x + 1,
 \end{aligned}
 \tag{4d}$$

which gives the four-tuple (0011) as the multiplication result.

The 16 four-tuples of the GF(2⁴) residue number field have been mentioned above already to give an impression of the set G. However, in order to “generate” the field *ab initio*, we have to use a primitive four-tuple, e.g., (0100) = x². We start with the element (0001) and proceed by multiplying with the mentioned primitive element. This is equivalent to multiplying each preceding four-tuple with x²,

$$\begin{aligned}
 (0001) &\rightarrow (0100) \rightarrow (0011) \rightarrow (1100) \rightarrow (0101) \rightarrow (0111) \\
 &\rightarrow (1111) \rightarrow (1001) \rightarrow (0010) \rightarrow (1000) \rightarrow (0110) \\
 &\rightarrow (1011) \rightarrow (1010) \rightarrow (1110) \rightarrow (1101).
 \end{aligned}
 \tag{5a}$$

The tuples reappear after the maximum number of possible steps, which is 15 = 2⁴ - 1 for m = 4. Thus, these sequences are called maximum number sequences.

To simplify the situation, we can also think of this number field as a binary-valued periodic sequence,

$$\{q_k\} = 1010111 \quad 10001001 \tag{5b}$$

(the gap is made for later reasons), of (2⁴ - 1) bits, if we just take the underlined least significant bit of all the 15 four-tuples from (5a). To identify the four-tuples of the sequence in Eq. (5b) we can successively observe the four subsequent bits to the right,

$$\begin{array}{l}
 \underbrace{101011110001001}_{a_0} \\
 \underbrace{101011110001001}_{a_1} \\
 \underbrace{101011110001001}_{a_2} \\
 \underbrace{101011110001001}_{a_3} \\
 \underbrace{101011110001001}_{a_4} \\
 \dots \\
 \underbrace{101011110001001}_{a_{11}} \\
 \dots \\
 101011110001001 \underbrace{1010}_{a_{14}} \dots \\
 101011110001001 \underbrace{1010}_{a_{15}=a_0} \dots
 \end{array}
 \tag{5c}$$

There is a recursion formula underlying this bit sequence (starting with the index k = 0 on the far left)—in this example,

$$q_{k+4} = q_{k+1} + q_{k+0}. \tag{6}$$

The recursion formula is related to the irreducible polynomial μ(x) = x⁴ + x + 1, which has been used to generate the sequence. As mentioned before, its zeroes stand for x⁴ = -(x + 1) = (x + 1) = x¹ + x⁰.

Side remark: If we had used the multiplication by (0010) = x instead of (0100) = x² in our example above, we would have achieved the same number sequence as in (5b) but starting at a different position, i.e.,

$$\{q_k\}_{\text{alternative}} = 10001001 \quad 1010111 \tag{7}$$

(now the reason for the gap in Eq. (5b) becomes clear).

C. Room frequency spectrum of Galois maximum number sequences

As mentioned before, 1D Galois fields have, e.g., been applied to concert hall acoustics (thus not related to electromagnetic but rather sound waves) as maximum number sequences. They have been realized as 1D reflecting surface reliefs. Such sequences repeat after the maximum number of permutations, e.g., in the GF(2⁴) case after all 2⁴ - 1 = 15 non-zero four-tuples or in a GF(2⁸) case after all 2⁸ - 1 = 255 non-zero eight-tuples.

Such structures have a pseudo-white 1D_x spatial frequency spectrum dependent on the spatial frequency ν_x. The prefix “pseudo” is used here because a number sequence is not continuous, but rather defined point-wise. Thus, the spatial frequency spectrum is defined point-wise too.

Analogous statements might be made for a corresponding 2D_{x,y} structure (as we will see) but now we are dealing with two spatial frequencies ν_x and ν_y and two scattering/diffraction angles β_x and β_y. Such a structure can either be considered as a complicated 2D_{x,y} diffraction grating or as the superposition of a large number of regular diffraction gratings with different grating constants g_x ~ 1/ν_x and g_y ~ 1/ν_y.

A special transformation has to be performed to map the 1D_x binary Galois number sequence onto a 2D_{x,y} array.

D. Mapping from 1D to 2D: The Sino representation

For improving concert hall acoustics with Galois scatterers, 1D structures would probably be sufficient most often since the ensemble of operagoers *usually* does not sit on many different levels. For this paper, both in the THz and in the optical regime, we would like to provide 2D scattering plates. Thus, a 1D sequence as in (5b) is not sufficient. In order to map the 1D sequence onto a 2D array with a pseudo-white spatial frequency spectrum in 2D, the Chinese remainder theorem (CRT) is helpful, which results in the so-called Sino representation.¹⁸ The CRT states that it is possible to reconstruct consecutive integers in a certain interval from their residues upon applying modulo functions, i.e., taking *modulo a set of coprime moduli*. The situation will be simple and easy to visualize if the number field has only two coprime factors because in this case, the residues and numbers can be arranged in a 2D list, which is exemplarily given further below.

If we take the set of 15 integers 0 to 14 (=15-1) as an example, which has the coprime factors 3 and 5 with 3 · 5 = 15, then any of these numbers can be reconstructed from the residues modulo 3 and 5. Again, as an example, let us assume that the residues are 1

and 2 [see inter-relations in (8)]; then it is clear that the sought-after integer number is 7. If the residues were 0 and 1, then the number would be 6,

- mod 3 – remainder & mod 5 – remainder ↔ number,
- 0 & 0 ↔ 0,
 - 1 & 1 ↔ 1,
 - 2 & 2 ↔ 2,
 - 0 & 3 ↔ 3,
 - 1 & 4 ↔ 4,
 - 2 & 0 ↔ 5,
 - 0 & 1 ↔ 6,
 - 1 & 2 ↔ 7,
 - 2 & 3 ↔ 8,
 - 0 & 4 ↔ 9,
 - 1 & 0 ↔ 10,
 - 2 & 1 ↔ 11,
 - 0 & 2 ↔ 12,
 - 1 & 3 ↔ 13,
 - 2 & 4 ↔ 14.

(8)

In mapping the Galois sequence from 1D to 2D and naming the two coprime numbers v and w , we can arrange the numbers in a $v \times w$ array/matrix/list. To illustrate this, it is helpful to rearrange the inter-relations in (8) into the list in Table I, with one remainder for the number modulo 3 and the second one for the number modulo 5.

The “geometrical” sequence of these 15 numbers in the list is illustrated with arrows in Table II.

The same “geometrical” sequence can and has to be applied for the 15 binary numbers from the exemplary 1D sequence in Eq. (5b), related to the binary residue number field $GF(2^4)$ (see Table III) and this is what is called the Sino-representation of the number sequence in Eqs. (5a)–(5c).

This very arrangement of numbers has a point-wise white spatial frequency spectrum both in the v_x - and in the v_y -direction, as had the 1D number sequence only in the v_x -direction. This is the

TABLE I. Mapping of the 1D residue Galois field with two coprime factors related to (8) into a 2D array/matrix/list.

mod5-remainder	= 0	= 1	= 2	= 3	= 4
mod3-remainder = 0	0	6	12	3	9
mod3-remainder = 1	10	1	7	13	4
mod3-remainder = 2	5	11	2	8	14

TABLE II. 2D list of the set of 15 numbers 0–14 from Table I with the sequence of numbers marked.

No. 0	No. 6	No. 12	No. 3	No. 9
No. 10	No. 1	No. 7	No. 13	No. 4
No. 5	No. 11	No. 2	No. 8	No. 14

TABLE III. “Geometrical” sequence of the 15 binary numbers from the exemplary 1D sequence in Eq. (5b), related to the residue number field $GF(2^4)$.

No. 0 = 1	No. 6 = 1	No. 12 = 0	No. 3 = 0	No. 9 = 0
No. 10 = 0	No. 1 = 0	No. 7 = 1	No. 13 = 0	No. 4 = 1
No. 5 = 1	No. 11 = 1	No. 2 = 1	No. 8 = 0	No. 14 = 1

reason why the Sino-representation is the optimum for scattering plate applications.

For applications in optics, we assume a circular light spot and, therefore, prefer a *geometrically nearly quadratic* (rather than extremely rectangular) 2D array with $v \approx w$ (the light spot is supposed to fit into the array, not having parts of the spot beyond the geometrical boundaries of the array). In addition, for high powers of 2, the number fields will have more than just two coprime moduli. In that case, a *weaker rule suffices* in order to allow for a *nearly* pseudo-white 2D spatial frequency spectrum, i.e., the two factors should be nearly equal, but they do not have to be primes. For example, for a number field $GF(2^{12})$, which has $2^{12} - 1 = 4095 = 63 \times 65$ elements, a 63×65 2D array will fulfill the task.

III. TECHNOLOGY FOR PREPARATION OF GALOIS PLATES

As stated before, for our scattering experiments, we used the binary residue number fields $GF(2^8)$, $GF(2^{10})$, and $GF(2^{16})$ as 2D arrays of 1’s and 0’s. They have been implemented via a 2D surface relief with a metallic top coating intended for use in reflection—nominally with $d = \lambda/2$ wide and $h = \lambda/4$ high mesas for the 1’s (and $\lambda/2$ wide voids with height 0).

A. 2D binary reflective THz Galois scattering plates

Figure 1 illustrates the technological process for preparation of a 2D binary reflective THz Galois scattering plate. The design frequency is 0.75 THz, equivalent to a vacuum wavelength of $\lambda = 400 \mu\text{m}$. Thus, any “bit” has a desired width of $d = \lambda/2 = 200 \mu\text{m}$, and in the case of 1’s/mesas, the desired height of $h = \lambda/4 = 100 \mu\text{m}$. Note that a refractive index or permittivity does not have to be considered since the final surface relief will have a metallic film as the uppermost layer and is intended for use in reflection.

The process is based on Ni electro-forming/plating because the latter gives dense and sinkhole-free metallic layers, and its spatial resolution suffices for the mentioned characteristic lateral bit size of $200 \mu\text{m}$.

The process starts with a bare Si wafer. A 10 nm thin Cr layer—intended as an adhesion-promotion agent—is deposited via electron-beam-evaporation onto the substrate. Then, a 200 nm thin Cu layer is deposited also via electron-beam-evaporation. It will serve as the lower electrode during the later Ni electro-forming step. A thick photoresist is spin-coated on top of the Cu layer and processed photolithographically, i.e., pre-baked, exposed through an appropriate exposure mask, developed, and post-baked. The photoresist is AZ[®]-125nXT by MicroChemicals, Ulm, Germany, especially developed for electro-forming processes. The structured photoresist layer is the structural basis for the Ni film, which is deposited during the subsequent electro-plating step. The Ni layer extends over

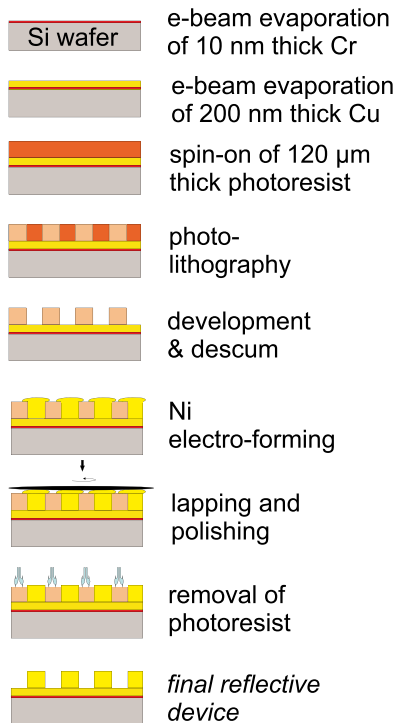


FIG. 1. THz scattering plate: sketch of the technological process for sample preparation. The thick photoresist is AZTM-125nXT by MicroChemicals, Ulm, Germany. The process is based on Ni electro-forming/plating because the latter gives dense and sinkhole-free metallic layers and its spatial resolution suffices to achieve the lateral feature size of 200 μm at 0.75 THz.

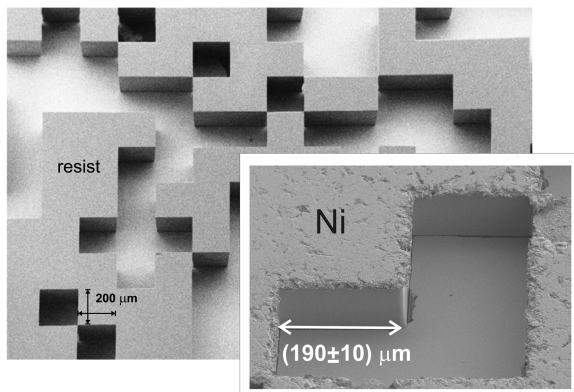


FIG. 2. THz GF(2⁸) 2D scattering plate with 15 × 17 = 255 elements: SEM micrographs of excerpts of the structured photoresist layer and (in the inset) of the final structured Ni layer (SEM = scanning electron microscope). The characteristic lateral width of any “bit” is nominally $d = \lambda/2 = 200 \mu\text{m}$. The SEM micrographs have each been taken under a non-zero angle with respect to the normal. The very good quality of the photoresist pattern is apparent. The final Ni structure shows a still acceptable roughness, especially at the top of the edges of the mesas. Due to the tolerances in etching, the experimentally achieved final characteristic lateral width is (190 ± 10) μm , which is accompanied by a 5% decrease as compared to the nominal value.

the entire photoresist structure such that it has to be lapped and polished until the photoresist mesas (inverse to the Ni mesas) are excavated again. Finally, the photoresist structure is etched away such that the structured Ni layer with its Ni mesas remains as the main part of the reflective device.

Figure 2 shows scanning electron microscope (SEM) images related to a THz GF(2⁸) scattering plate nominally optimized for a frequency of 0.75 THz. The micrographs show just an excerpt of the structured photoresist layer after processing and, in the inset, an even smaller part of the final structured Ni layer. The characteristic lateral width of any “bit” should be $d = \lambda/2 = 200 \mu\text{m}$. The very good quality of the photoresist pattern is obvious. The final Ni structure shows a still acceptable roughness, especially at the top of the edges of the mesas. Due to the tolerances in etching, the experimentally achieved final characteristic lateral width is (190 ± 10) μm , which is accompanied by a 5% decrease as compared to the nominal value. Thus, the optimal wavelength is reduced by 5% as compared to the design wavelength. Hence, the optimal frequency is increased by 5%.

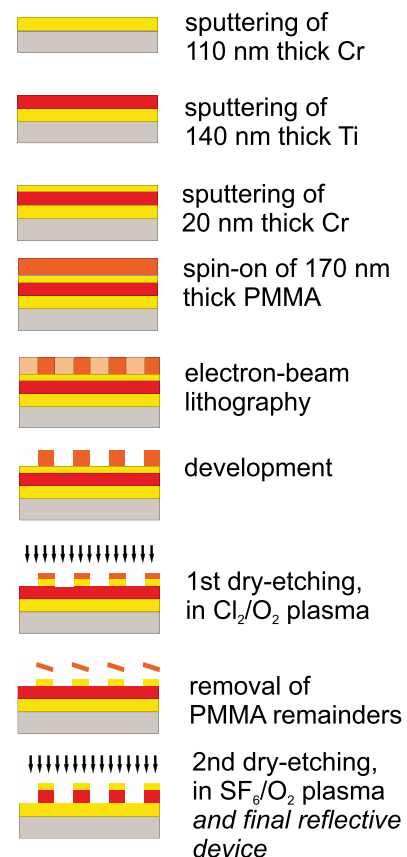


FIG. 3. Optical frequency scattering plate: sketch of the technological process for sample preparation. The procedure is explained in more detail in the text. PMMA (polymethylmethacrylate) 950 K 4% from Allresist, Strausberg, Germany, is used as the e-beam-lithographic resist. E-beam lithography is necessary due to the desired better resolution than in the THz case.

B. 2D binary reflective optical Galois scattering plates

Figure 3 gives a sketch of the technological process for sample preparation of a 2D binary reflective optical frequency (“optical”) Galois scattering plate. Before the resist layer is applied, a metallic three-layer sequence (Cr-Ti-Cr) has to be deposited. Such three-layer stacks allow for steeper flanks upon dry-etching and, thus, for better shape accuracy. PMMA (polymethylmethacrylate) 950 K 4% from Allresist, Strausberg, Germany, is used as the e-beam-lithographic resist. After exposure, development, and fixation, i.e., after the processing of the resist layer, it acts as a soft etch mask for a first main dry-etch step, which is used to structure the upper Cr layer. Then, the latter acts as a hard etch mask in a second main dry-etch step. After the first etch step, the residues of the resist are removed (in an intermediate etch step). In the second main etch step, the Ti layer is structured, leading to the final reflective device with Cr as its upper metal everywhere on the surface, i.e., on the Ti mesas as well as in-between.

The design wavelength λ of these “optical” reflective Galois scattering plates has been either 642 or 800 nm, being the emission wavelengths of semiconductor laser diodes to be used for the scattering measurements.

Figures 4 and 5 contain SEM micrographs of the PMMA pattern of a binary 2D GF(2¹⁶) number field (design wavelength $\lambda = 642$ nm) and a cut-out of a final Cr pattern, again of a binary 2D GF(2¹⁶) number field (but for $\lambda = 800$ nm), respectively. The structures are of good quality and spatial resolution.

In order to match the area of the scattering plates as well as possible to the area of the spot of radiation, we typically stitch/tile many Galois plates to one another into a 2D square array. In the case of a scattering plate from the GF(2¹⁶) number sequence, we employ a 16×16 stitching array of $\nu \times w = 255 \times 257$ Galois bit arrays. In cases with GF(2⁸), a 256×256 stitching array of the $\nu \times w = 15 \times 17$ Galois bit arrays is used. As an undesired consequence, the stitching introduces a periodicity with a large grating constant into the scattering plate. However, the corresponding spatial frequency is the

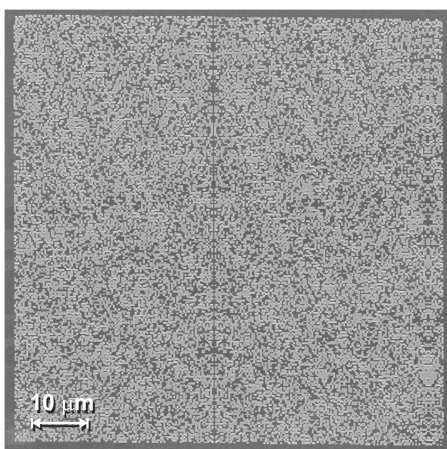


FIG. 4. Optical frequency GF(2¹⁶) 2D scattering plate with 4096 sixteen-tuples or $255 \times 257 = 65\,535$ bits: the SEM micrograph of the PMMA pattern after processing. The design wavelength is 642 nm.

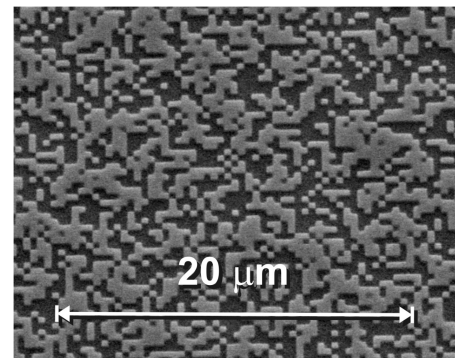


FIG. 5. Optical frequency GF(2¹⁶) 2D scattering plate with $255 \times 257 = 65\,535$ bits: cut-out of the SEM micrograph of the Cr pattern after the complete technological process. The design wavelength is 800 nm here.

smallest occurring spatial frequency, adding only a fine structure to the distribution of diffracted intensity.

IV. THEORETICAL EXPECTATIONS EXEMPLARILY FOR THE OPTICAL CASE¹⁶

Figures 6–8 show theoretical results, which have been obtained using MatLabTM by The MathWorks, Natick, MA, USA, according to Kirchhoff’s diffraction theory for an ideal optical binary 2D Galois plate of type GF(2⁸) and a wavelength of 642 nm for normal incidence.

How many scattering/diffraction orders can be expected? For normal radiation incidence, the diffraction angle β is given by

$$\sin \beta = r \frac{\lambda}{d}, \quad (9a)$$

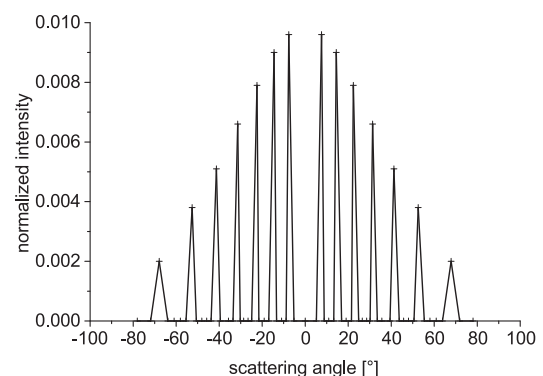


FIG. 6. Optical frequency 2D binary scattering plate, ideal, GF(2⁸), $\lambda = 642$ nm, normal incidence: numerical result and normalized intensity as a function of angle of detection (scattering angle). The calculation has been performed under the assumption of an optimal width d of the mesas of $\lambda/2$ in both lateral dimensions. Thus, $d/\lambda = 0.50$. The assumed mesa height is $h = \lambda/4$. The lines are only guides to the eye.

with the diffraction order r and the grating constant d . Even for $r = 1$, no diffraction order at all should be expected for $d/\lambda = 0.5$ or $\lambda/d = 2$ because the absolute value of the sine function cannot be larger than 1.

However, since Galois fields are based on maximum number sequences, there is a larger grating constant (beyond d), i.e., $v \cdot d$. Thus, Eq. (9a) has to be rewritten as

$$\sin \beta = r \frac{\lambda}{v \cdot d}. \quad (9b)$$

In the case of $\text{GF}(2^8)$, an array of $v \times w = 15 \times 17$ bits has to be considered; hence,

$$\sin \beta = r \frac{\lambda}{15 \cdot d}. \quad (9c)$$

Thus, for $d/\lambda = 0.5$ or $\lambda/d = 2$, the absolute value of r as a whole number has to be smaller than or equal to $v/2 = 15/2$, i.e.,

$$|r| \leq \text{int}\left(\frac{v}{2}\right) = \text{int}\left(\frac{15}{2}\right) = \text{int}(7.5) = 7 \quad (9d)$$

and $|r_{\max}| = 7$. Thus, seven maxima should be expected in this example on each side of the zeroth order—in cases where d/λ has the ideal value of 0.5.

However, this also illustrates that a different number of maxima should be expected as soon as d/λ is not 0.5.

Figure 6 shows the calculated normalized scattering intensity dependent on the angle of detection, i.e., the scattering angle. The calculation has been performed under the assumption of an *optimal width d of the mesas of $\lambda/2$* (\rightarrow factor $1/2$ below) in both lateral dimensions. Thus, for the $\text{GF}(2^8)$ plate, there should be and indeed are seven maxima on each side of the specular direction. The specular peak should (nearly) vanish, as long as each mesa has the optimum height and ideally steep flanks. The lines in Fig. 6 are only guides to the eye.

Figure 7 shows the result from Fig. 6 in a polar diagram with the normalized intensity on a logarithmic scale. The broadening of the point maxima to dashes is due to an integration over

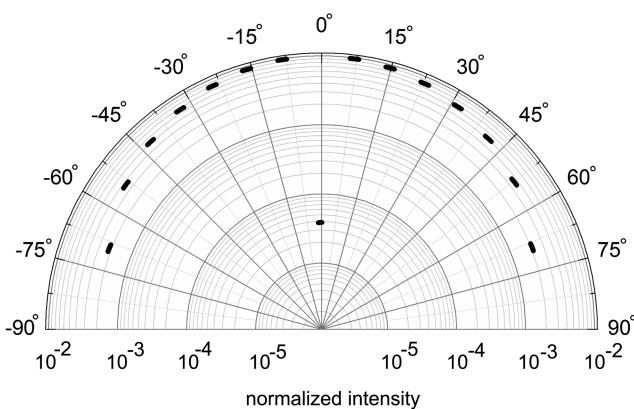


FIG. 7. Optical frequency 2D binary scattering plate, ideal, $\text{GF}(2^8)$, $\lambda = 642$ nm: numerical result related to Fig. 6, the polar diagram with the normalized intensity on a logarithmic scale, the detector width taken into account.

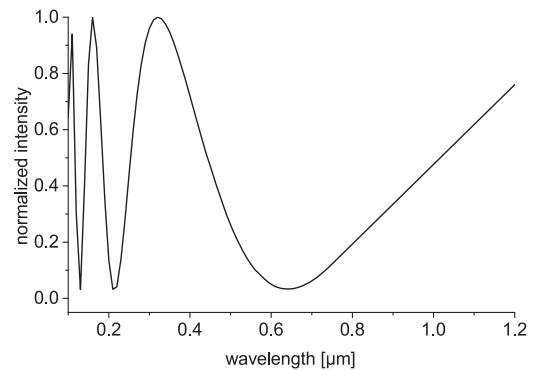


FIG. 8. Optical frequency 2D binary scattering plate, ideal, $\text{GF}(2^8)$, $\lambda = 642$ nm: numerical result just for the specular direction. As expected for $h = \lambda/4$ in reflection, a minimum appears for the design wavelength of 642 nm.

a certain angle of detection, corresponding to the width of the (numerically assumed) photodetector intended for use. A small specular peak can be recognized when observed carefully. At this point in time, we cannot identify its reason clearly, but we assume that it is related to sampling errors (discretization in the lateral dimensions).

Figure 8 shows the ideal $\text{GF}(2^8)$ Galois scattering plate, just dealing with the specular direction (no deflection). This figure reveals that indeed a minimum intensity can be expected for the design wavelength of 642 nm for $h = \lambda/4$ and a reflective device.

V. EXPERIMENTAL SETUPS AND RESULTS

Earlier in this paper, stitching/tiling has already been mentioned as a means to match the scattering plate area with the area of the spot of radiation as much as possible. In the optical case, the laser spot diameter is 1 mm, while the area of the stitched array is about $1.3 \times 1.3 \text{ mm}^2$. Thus, the laser spot fits completely onto the stitched Galois scattering plate. Even in the THz case, stitching/tiling is applied; however, during the measurements reported here, the THz radiation is focused and the focal area is nearly identical to a single Galois tile (sub-array).

As also mentioned before, of course, this tiling or stitching introduces another (a large) grating constant, which also causes a non-zero scattering intensity in the specular direction (i.e., in the zeroth order).

A. THz setup and results

Figure 9 presents the photographic (nearly) top-view of the THz scattering setup. It has been built and operated by the TeraTec group of the Fraunhofer IPM Institute in Kaiserslautern, Germany. It includes an emitter with a mean frequency of 0.75 THz. The emitter is positioned at -20° with respect to the sample normal. Moreover, there is the sample holder and a slewable detector, making the setup a one-axis goniometer.

Figure 10 shows a diagram of the scattering intensity as a function of the scattering angle for a fixed frequency of 0.75 THz. Due

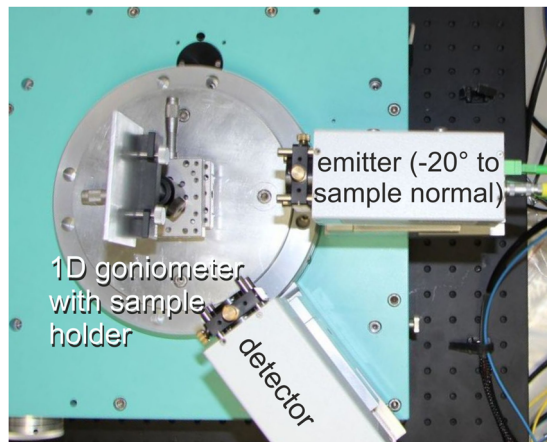


FIG. 9. THz scattering measurements: (nearly) top-view of the THz measurement setup. It has been implemented and operated by the TeraTec group of the Fraunhofer IPM Institute in Kaiserslautern, Germany. It includes an emitter at -20° with respect to the sample normal, the sample holder, and the detector. The emitter radiates with a mean frequency of 0.75 THz.

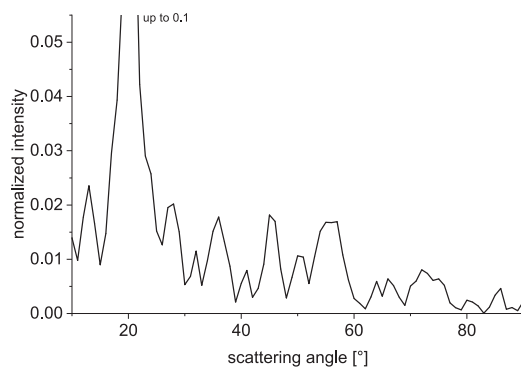


FIG. 10. THz scattering measurements of the GF(2^{10}) plate: scattering intensity as a function of the scattering angle for a fixed frequency of 0.75 THz. The wavelength is $\lambda = 400 \mu\text{m}$. The desired mesa widths have been $d = \lambda/2 = 200 \mu\text{m}$ in both lateral dimensions, but according to Fig. 2 [there for a GF(2^8) plate], the actual widths are $d = (190 \pm 10) \mu\text{m}$. The mesa heights are $h = \lambda/4 = 100 \mu\text{m}$. Due to fabrication imperfections of the mesas, the zeroth order (to be observed for the specular angle of $+20^\circ$) is still quite strong. According to Eq. (9b), a number of $\text{int}(31/2) = 15$ maxima should be expected on each side of the specular peak. Taking any small peak to the right of the zeroth peak in the diagram, one might count 14 maxima.

to fabrication imperfections of the mesas, the zeroth order (to be observed for the specular angle of $+20^\circ$) is still quite strong.

Underlying this result is reflective scattering from a GF(2^{10}) 2D scattering field with ($1024 = 31 \times 33$) bits. According to Eq. (9b), this implies that $\text{int}(31/2) = 15$ maxima should be expected on any side of the specular peak. Taking any small peak to the right of the zeroth peak in the Fig. 10, one might count 14 maxima. However, it is not astonishing that the diffraction efficiency is also reduced by fabrication imperfections so that one (or some) orders are strongly diminished.

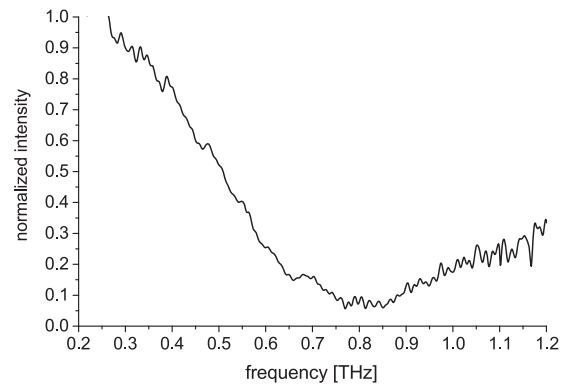


FIG. 11. THz scattering measurements for the GF(2^8) plate: The result is achieved for an angle of detection of $+20^\circ$, i.e., for specular reflection. The minimum appears for (0.79 ± 0.02) THz, which is related to a 5% increase as compared to the theoretical value. In addition, this corresponds to the 5% decrease in the characteristic width d from that shown in Fig. 2 as compared to the desired value of $200 \mu\text{m}$. Data are taken from our own publication.¹⁵

In Fig. 11, an experimentally obtained THz spectrum in reflection is given, which has been achieved with a THz scattering plate with GF(2^8), also for an angle of incidence of -20° . The angle of detection is fixed at $+20^\circ$, which corresponds to the specular direction. For the specular reflection, a minimum should be expected for the design wavelength of 0.75 THz. However, the minimum appears for (0.79 ± 0.02) THz, which is related to a 5% increase as compared to the theoretical value. In addition, this corresponds to the 5% decrease in the characteristic width d from that shown in Fig. 2 as compared to the desired value of $200 \mu\text{m}$.

In a partially qualitative, partially quantitative sense, the experimentally obtained graph shown in Fig. 10 can, in principle, be compared to the calculated result in Fig. 6 since the width and the height of the mesas are (nearly) ideal, i.e., $d/\lambda = 0.5$, $h = \lambda/4$, in both cases. The latter are scaled versions of each other. Beyond the influence of fabrication imperfections, the quantitative difference in the number of expected as well as received scattering maxima is due to the fact that Fig. 6 deals with a scattering plate based on GF(2^8), while Fig. 10 is related to GF(2^{10}).

In Fig. 12, a result will be given, which is based on a GF(2^8) case, where the mesa width is not $d/\lambda = 0.50$ but rather $d/\lambda = 0.86$. Thus, Fig. 12 might be compared to Fig. 6 to reveal the influence of d/λ on the number of scattering maxima.

According to Eqs. (9a) and (9b), a value of $d/\lambda = 0.86$ should lead to a number of 14 scattering maxima on both sides of the specular peak (instead of 7 in Fig. 6). This finding might be considered an opportunity for manipulation of the number of scattering maxima. However, it has to be kept in mind that in a non-ideal case (i.e., $d/\lambda > 0.5$), the diffraction efficiency of the zeroth (specular) order will be increased, and the diffraction efficiencies of any higher order (i.e., $|r| > 0$) will be reduced (due to the non-ideality and due to the larger number of scattering maxima/diffraction orders).

B. Optical frequency setup and results

The setup for the measurements at optical frequencies is again a one-axis goniometer. The semiconductor laser emits linearly

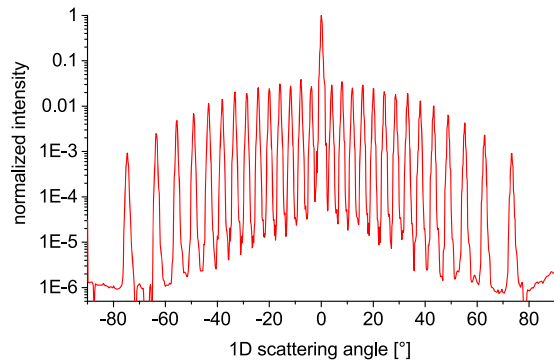


FIG. 12. Scattering measurements for the optical frequency range, GF(2⁸)—qualitatively comparable to the result given in Fig. 6: the multiplicity of maxima can be clearly observed. The emission wavelength λ of the semiconductor laser is 642 nm, and the mesa width d is 550 nm in both lateral dimensions, i.e., $d/\lambda = 0.86$. The mesa height is $h = \lambda/4$.

polarized light. A half-wave plate and a polarizer are used to provide two different planes/directions of linear polarization. However, no differences in the results could be observed for different planes of linear polarization.

As discussed in connection to Eqs. (9a)–(9d), the number of maxima (diffraction orders beyond the zeroth one) is not only related to the quantity ν of the $\nu \times w$ array but also to the ratio λ/d . Ideally, this ratio should be $\lambda/d = 2$ or $d/\lambda = 0.5$. To show the influence of deviations of the latter's ratio from the value 0.5, we deliberately used a non-ideal ratio. According to Eqs. (9a)–(9d), this measure can be used to manipulate the number of maxima.

Results are given here for a GF(2⁸) plate and a laser of an emission wavelength of $\lambda = 642$ nm. With mesa width $d = 550$ nm (instead of 321 nm), the ratio is $d/\lambda = 0.86$ (instead of 0.50). The device is a $\nu \times w = 17_{\text{horizontal}} \times 15_{\text{vertical}}$ array. In that case, according to

$$\sin \beta = r \frac{1}{\nu \cdot 0.86} = r \frac{1}{17 \cdot 0.86} = r \frac{1}{14.6}, \quad (9e)$$

$|r_{\text{max}}| = 14$ should be expected on each side of the specular direction.

This expectation is verified by the experiment. In Fig. 12, a 1D cut through the plane of detection, through the optical axis, and through the observable maxima is shown, *horizontal* and centered on the zeroth order, with 14 maxima on each side of the specular direction. The specular reflection peak is not negligible since there has been stitching of Galois structures and non-ideal mesa flanks. Hence, the intensities of all higher orders (i.e., $|r| > 0$) are diminished.

Moreover, it has to be stressed that the diffraction efficiencies of any order, including the zeroth one, also depend on the number of existing orders. Thus, there is a trade-off between the diffraction intensity of the zeroth order (i.e., the specular reflection) and the number of other orders. More clearly, the fewer diffraction orders exist, the larger will be the intensity of specular reflection.

The Galois plate concept clearly works even for optical frequencies, and through (deliberate) deviation from the condition $d/\lambda = 0.5$, the number of diffraction orders can be changed considerably.

VI. CONCLUSIONS

In this paper, we have emphasized the mathematical design basis as well as the technological fabrication processes to prepare binary residue 2D Galois scattering plates—both for the THz range and for the optical frequency range. As in Refs. 14–16, we have verified the theoretically expected scattering behavior by experimental results. The scattering intensity distributions incorporate a multitude of maxima.

By varying the mesa (bit) width d or the wavelength λ , the number of scattering maxima (diffraction orders) can be varied strongly. However, diffraction efficiency for all orders will be diminished if the number of orders is increased by applying ratios $d/\lambda > 0.5$.

By fabricating multilevel scattering plates instead of binary ones, the range of operating frequencies/wavelengths could be broadened¹⁸—also at the expense of diffraction efficiency.

THz and optical Galois scattering plates offer another opportunity to the tool box of scattering plates.

ACKNOWLEDGMENTS

The authors would like to thank the German Research Foundation (DFG, Deutsche Forschungsgemeinschaft) for financial support under Contract No. FO157/39; Sandra Wolff, Head of the Nanostructuring Center (NSC) at Technische Universität Kaiserslautern (TUK), for general support; and the NSC for special support. Assistance from “Forschungsinstitut fuer mineralische und metallische Werkstoffe – Edelsteine/Edelmetalle” (FEE), Idar-Oberstein, Germany (lapping and polishing), is also gratefully acknowledged. Daniel Molter, TeraTec group of Fraunhofer IPM, Germany (THz measurements); Simon Ediger and Monika Saumer, University of Applied Sciences Kaiserslautern/Zweibruecken, Germany (electroplating); and Stefan Trellenkamp as well as Juergen Moers, FZ Juelich, Germany (patterning and etching of the optical plate) are also gratefully acknowledged.

H.F. would also like to thank M. R. Schroeder (deceased 2009)^{18–20} for his brilliant lectures, where he introduced the concept of acoustical Galois scattering plates to his students.

The authors declare that there is no conflict of interest.

DATA AVAILABILITY

The data that support the findings of this study are available from the corresponding author upon reasonable request.

REFERENCES

- E. Hein, “Optically scattering glass surface roughnesses due to self-masking during dry-etching,” Ph.D. thesis, Physics Department, Technische Universität Kaiserslautern (TUK); Verlag Dr. Hut, 2011 (in German).
- S. Y. Lee, G. F. Walsh, and L. Dal Negro, “Microfluidics integration of aperiodic plasmonic arrays for spatial-spectral optical detection,” *Opt. Express* **21**(4), 4945–4957 (2013).
- R. A. Lewis, “A review of terahertz sources,” *J. Phys. D: Appl. Phys.* **47**, 374001 (2014).
- J. Federici and L. Moeller, “Review of terahertz and subterahertz wireless communications,” *J. Appl. Phys.* **107**, 111101 (2010).
- T. Kleine-Ostmann and T. Nagatsuma, “A review on terahertz communications,” *J. Infrared, Millimeter, Terahertz Waves* **32**, 143–172 (2011).

- ⁶M. Hangyo, M. Tani, and T. Nagashima, "Terahertz time-domain spectroscopy of solids: A review," *Int. J. Infrared Millimeter Waves* **26**(12), 1661–1690 (2005).
- ⁷M. Naftaly, N. Vieweg, and A. Deninger, "Industrial applications of terahertz sensing: State of play," *Sensors* **19**, 4203 (2019).
- ⁸F. Ellrich, M. Bauer, N. Schreiner, A. Keil, T. Pfeiffer, J. Klier, S. Weber, J. Jonuscheit, F. Friederich, and D. Molter, "Terahertz quality inspection for automotive and aviation industries," *J. Infrared, Millimeter, Terahertz Waves* **41**, 470–489 (2020).
- ⁹E. Hein, D. Fox, and H. Fouckhardt, "Self-masking controlled by metallic seed-layer during glass dry-etching for optically scattering surfaces," *J. Appl. Phys.* **107**(3), 033301 (2010).
- ¹⁰H. Fouckhardt, I. Steingoetter, M. Brinkmann, M. Hagemann, H. Zarschizky, and L. Zschiedrich, "nm- and μm -scale surface roughness on glass with specific optical scattering characteristics on demand," *Adv. OptoElectron.* **2007**, 27316.
- ¹¹H. Fouckhardt, E. Hein, D. Fox, and M. Jaax, "Multitude of glass surface roughness morphologies as a tool box for dosed optical scattering," *Appl. Opt.* **49**(8), 1364–1372 (2010).
- ¹²E. Hein, D. Fox, and H. Fouckhardt, "Glass surface modification by lithography-free reactive ion etching in an Ar/CF₄-plasma for controlled diffuse optical scattering," *Surf. Coat. Technol.* **205**(2), S419–S424 (2011).
- ¹³E. Hein, D. Fox, and H. Fouckhardt, "Lithography-free glass surface modification by self-masking during dry-etching," *J. Nanophotonics* **5**, 051703 (2011).
- ¹⁴M. Jaax, B. Laegel, S. Wolff, and H. Fouckhardt, "Optical reflective Galois scattering plates," in Proceedings of the European Optical Society Annual Meeting (EOSAM) 2012, Aberdeen, 2012, contribution TOM3_5920_009.
- ¹⁵M. Jaax, S. Wolff, B. Laegel, and H. Fouckhardt, "Optical and THz Galois diffusers," *J. Eur. Opt. Soc.* **8**, 13020 (2013).
- ¹⁶M. Jaax, "Optical and terahertz Galois scattering plates," Ph.D. thesis, Physics Department, Technische Universität Kaiserslautern (TUK); Verlag Dr. Hut, 2013; 2014 (in German).
- ¹⁷Y. K. S. Lee, "Engineering aperiodic nanostructured surfaces for scattering-based optical devices," Ph.D. thesis, College of Engineering, Boston University, 2013.
- ¹⁸M. R. Schroeder, *Number Theory in Science and Communication*, 4th ed. (Springer, 2006).
- ¹⁹M. R. Schroeder, "Number theory and the real world," *Math. Intell.* **7**(4), 18–26 (1985).
- ²⁰M. R. Schroeder, "The unreasonable effectiveness of number theory in science and communication (1987 Rayleigh lecture)," *IEEE ASSP Mag.* **1988**, 5–12.
- ²¹W. Stahnke, "Primitive binary polynomials," *Math. Comput.* **27**(124), 977–980 (1973).